Available online at www.sciencedirect.com
ScienceDirect
Journal of Power Sources 175 (2008) 595–603
JOURNAL OF POWER SOURCES
www.elsevier.com/locate/jpowsour

The roles of cellular and dendritic microstructural morphologies on the corrosion resistance of Pb–Sb alloys for lead acid battery grids

Wislei R. Osório, Daniel M. Rosa, Amauri Garcia *

Department of Materials Engineering, State University of Campinas-UNICAMP, PO Box 6122, 13083-970 Campinas, SP, Brazil

Received 2 August 2007; received in revised form 21 August 2007; accepted 31 August 2007
Available online 4 September 2007

Abstract

During the past 20 years, lead acid batteries manufacturers have modified grid manufacturing processes and the chemical composition of the used alloys in order to decrease battery grid weight as well as to reduce the production costs, and to increase the battery life-time cycle and the corrosion resistance. The aim of this study was to evaluate the effects of cellular and dendritic microstructures of two different Pb–Sb alloys on the resultant corrosion behavior. A water-cooled unidirectional solidification system was used to obtain cellular and dendritic structures. Macrostructural and microstructural aspects along the casting have been characterized by optical microscopy and SEM techniques. Electrochemical impedance spectroscopy and potentiodynamic polarization curves were used to analyze the corrosion resistance of samples in a 0.5 M H_2SO_4 solution at 25 °C. For cellular microstructures the corrosion rate decreases with increasing cell spacing. In contrast, finer dendritic spacings exhibit better corrosion resistance than coarser ones. The microstructural pre-programming may be used as an alternative way to produce Pb alloy components in conventional casting, rolled-expanded, and continuous drum casting with better corrosion resistance.

Keywords: Pb–Sb alloy; Battery grids; Cellular microstructure; Dendritic microstructure; Corrosion resistance

1. Introduction

A variety of grid manufacturing processes [1–3] have been used by many battery manufacturers to decrease battery grid weight as well as to reduce the production costs, and to increase the battery life-time cycle and the corrosion resistance [3,4]. A battery grid must be dimensionally stable and have mechanical properties, which can resist the stresses of the charge/discharge reactions without bending, stretching or warping. The structural and mechanical characteristics of lead–antimony alloys as well as their precipitation hardening effect make them a very convenient material for lead acid battery positive grids [5–8]. The antimony content of a Pb–Sb electrode affects the mechanical properties, the microstructure, the electrochemical behavior of active materials and corrosion layers on the electrode [3]. The corrosion resistance of Pb alloys is an important characteristic not only when the grids performance is concerned but also in pasting and curing. Prengaman [3] has reported that for Pb–Sb grid alloys, the antimony content increases the rate of oxidation of lead, both at the grain boundary as well as inside the matrix grains. Typical Pb–Sb grid and pasted negative and positive plates are shown in Fig. 1.

In the early 1980s, a number of metallurgists, physicists and mathematicians have investigated the interface morphologies in which the cellular/dendritic growth is one of the most complicated solidification patterns [9–13]. The cellular and dendritic spacings are important microstructural parameters affecting the microscopic segregation between these ramifications, mechanical properties, and particularly, the dendritic spacing has strongly influenced the overall surface corrosion resistance of binary alloys [14,15]. Generally, the growth of regular cells is favored by low growth rates during solidification and/or low solute content. On the other hand, dendritic arm spacings are typical of alloys with higher solute content and/or solidified under higher growth rates. Some studies existing in literature have focused on the characterization of cellular and dendritic growth of Pb–Sb dilute alloys [9–13,15]. In a recent article [15], it was found that coarser cellular structures tend to yield higher corrosion resistance than finer cellular structures for a Pb–0.85 wt% Sb alloy. Such tendency was associated with

* Corresponding author. Tel.: +55 19 3521 3320; fax: +55 19 3289 3722.
E-mail address: amaurig@fem.unicamp.br (A. Garcia).

0378-7753/$ – see front matter © 2007 Elsevier B.V. All rights reserved.
doi:10.1016/j.jpowsour.2007.08.091

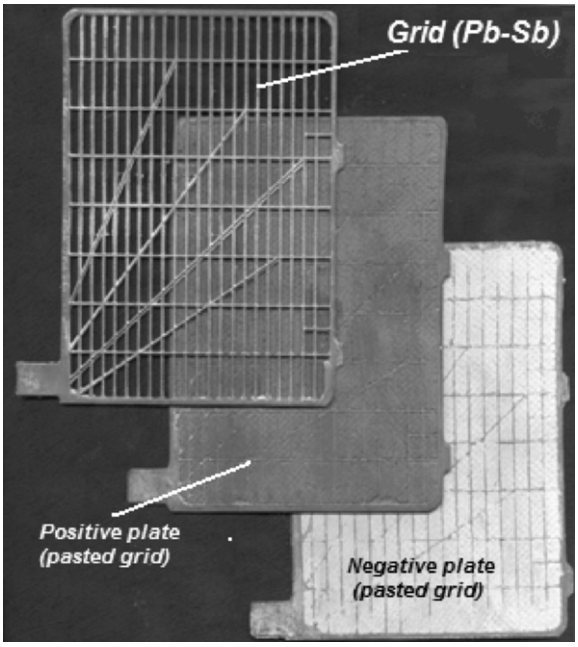

Fig. 1. Pb–Sb grid and pasted negative and positive plates used in a typical lead acid battery.

the reduction of cellular boundaries when compared with finer cells, since the boundary has proved to be more susceptible to the corrosion action.

Some recent studies have shown that the improvement on the corrosion resistance depends on the cooling rate imposed during solidification (which affects dendrite arm size and solute redistribution) and on the electrochemical behavior of solute and solvent [15–19]. In order to get an as-cast grid with better electrochemical behavior, the control of cooling rate is very important since it affects the grid microstructure and consequently its corrosion resistance [14–19]. It has been reported [3,6] that lower cooling rates during solidification of a lead–antimony alloy casting have provided antimony segregation to the interior of the casting while antimony concentration at the casting surface has significantly decreased.

The aim of this study was to evaluate the different mechanisms and tendencies of corrosion action on cellular microstructures of a dilute Pb–Sb alloy and on dendritic microstructures of a more concentrated Pb–Sb alloy. For this purpose, a water-cooled unidirectional solidification system was used to obtain controlled solidified samples. Such experimental set-up has permitted the imposition of a wide range of cooling conditions and hence a wide spectrum of cellular and dendritic spacings could be analyzed. Corrosion tests were carried-out with samples in a 0.5 M H_2SO_4 solution at 25 °C in a pH range from 0.88 to 0.96.

2. Experimental procedure

2.1. Specimens preparation

The alloys (Pb–0.85 and 6.6 wt% Sb) were prepared from commercially pure metals: Pb (99.97 wt%) and Sb (99.86 wt%). The solute contents of 0.85 and 6.6 wt% Sb were chosen in order to provide cellular and dendritic structures, respectively.

A water-cooled unidirectional solidification system was used in the experiments. The solidification set-up was designed in such way that the heat was extracted only through the water-cooled bottom, promoting vertical upward directional solidification. From the water-cooled bottom to the top of the unidirectionally solidified ingot a wide range of cooling rates were obtained since the efficiency of heat extraction decreases with the distance from the ingot bottom. Such thermal behavior affects cells and dendrites arm spacings along the ingot. More details concerning this solidification set-up can be obtained in a previous article [15].

The cylindrical ingot was sectioned on a midplane, grinded, polished and etched with a solution to reveal the macrostructure. Transverse sections (perpendicular to the growth direction) from the directionally solidified specimen along the ingot length were polished and etched with a solution (37.5 mL of glacial acetic acid and 15 mL of H_2O_2, at 25 °C) for microscopy examination. Image processing systems Neophot 32 (Carl Zeiss, Esslingen, Germany) and Leica Quantimet 500 MC (Leica Imaging Systems Ltd., Cambridge, England) were used to measure both cellular and dendritic spacings. The macrosegregation profile was determined by a scanning electron microscope (SEM, JMS T20 of Jeol Co., Japan) and an energy dispersive X-ray analyzer (EDAX, NORAN, System Six 1.5, USA).

2.2. Corrosion tests

It is important to remark that the corrosion behavior analysis of the present work differs from studies of PbO/PbO_2 formation which consider the corrosion of the lead electrode and proceed at much higher potentials. The analysis also differs from studies of $PbSO_4$ membrane layer formed on the electrode surface which in a 0.5 M H_2SO_4 solution presents high solubility, as detailed in the literatures [20,21].

In order to evaluate the overall corrosion behavior of the microstructural cellular and dendritic morphologies, electrochemical impedance spectroscopy (EIS) and potentiodynamic polarization tests were carried-out on samples collected at different positions along the casting length. The EIS tests were carried-out in a 500 mL of sulfuric acid solution (0.5 mol L^{-1}) at 25 °C. A potentiostat coupled to a frequency analyzer system, a glass corrosion cell kit with a platinum counter electrode and a saturated calomel reference electrode (SCE) were used. The working electrodes consisted of casting alloy samples, which were positioned at the glass corrosion cell kit, leaving a circular 1 cm^2 metal surface in contact with the electrolyte. The potential amplitude was set to 10 mV in open-circuit potential and the frequency range was set from 100 mHz to 100 kHz. The samples were further ground to a 600 grit SiC finish, followed by distilled water washing and air-drying before measurements. EIS measurements began after an initial delay of 30 min for the sample to reach a steady-state condition.

Polarization tests were also carried-out in a 500 mL of sulfuric acid solution (0.5 mol L^{-1}) at 25 °C using an EG&G Princeton Applied Research, model 273A potentiostat at a scan rate of

0.2 mV s^{-1} from −250 mV (SCE) to +250 mV (SCE) related to open-circuit potential. Using an automatic data acquisition system, the potentiodynamic polarization curves were plotted and both corrosion rate and potential were estimated by Tafel plots [23]. The EIS experimental results were analyzed by equivalent circuits which were proposed by using the ZView software.

3. Results and discussion

3.1. Microstructure and cooling rate

Fig. 2a shows the resultant directionally solidified casting macrostructure. It can be seen that the growth of columnar grains prevailed along the entire casting length due to the water-cooled unidirectional system and the solidification conditions used in the experiments.

The positions along the casting from where the samples for corrosion tests were collected are shown in Fig. 2a. Cellular spacing (λ_1) and secondary dendritic arm spacing (λ_2) are also shown in Fig. 2a corresponding to each position from the casting/chill surface (from the bottom to the casting top).

As a result of the high efficiency of the imposed heat extraction, especially at the first stages of solidification (bottom region), a wide range of cooling rates could be attained along the casting length. The experimental cooling rate dependences on cellular and dendritic (secondary dendrite arm spacing) structures are shown in Fig. 2b, where average spacings along with the standard variation are presented. The line represents an empirical power law which fits the experimental points.

It can be seen in Fig. 2b that the use of a water-cooled mold imposes higher values of cooling rates near the casting/chill

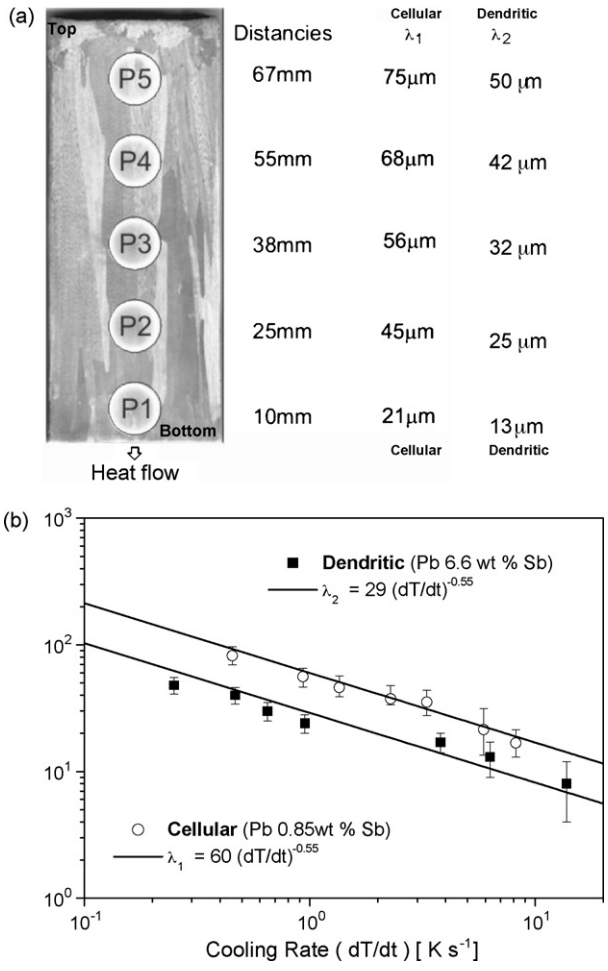

Fig. 2. (a) Typical directionally solidified macrostructure of Pb–Sb alloy showing positions from where samples were collected for corrosion tests and the corresponding mean values of cell and secondary dendrite arm spacings. (b) Typical cellular and secondary dendrite arm spacings as a function of cooling rate.

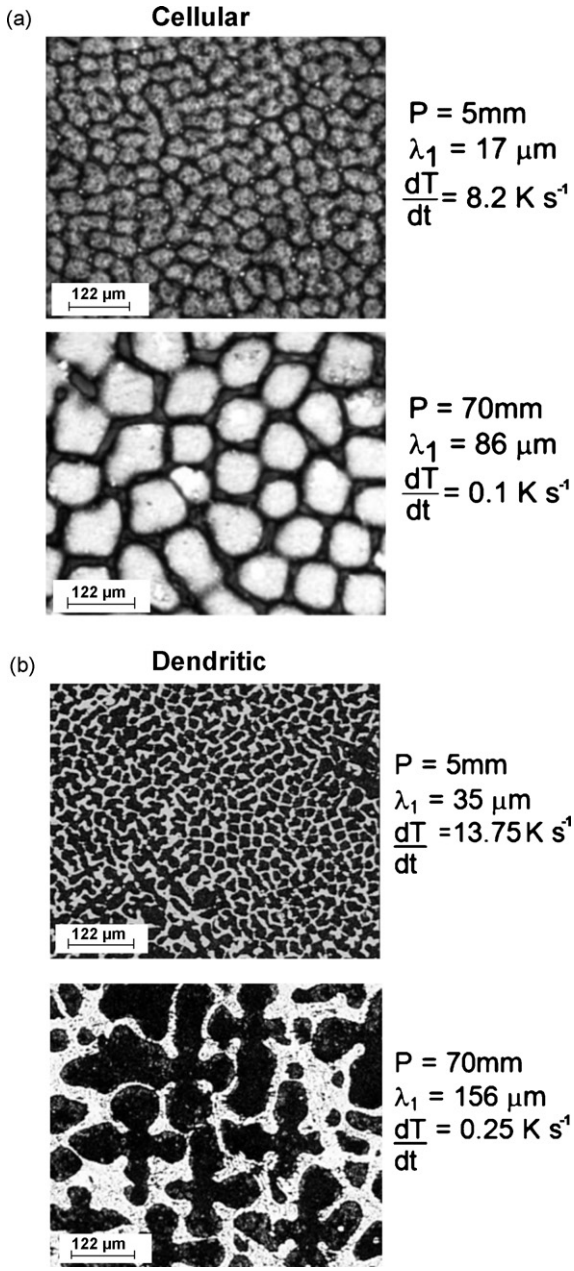

Fig. 3. (a) Typical optical microscopy images at 5 and 70 mm from the casting/chill surface (cross-section): cellular microstructure (Pb–0.85 wt% Sb). (b) Typical optical microscopy images at 5 and 70 mm from the casting/chill surface (cross-section): dendritic microstructure (Pb–6.6 wt% Sb).

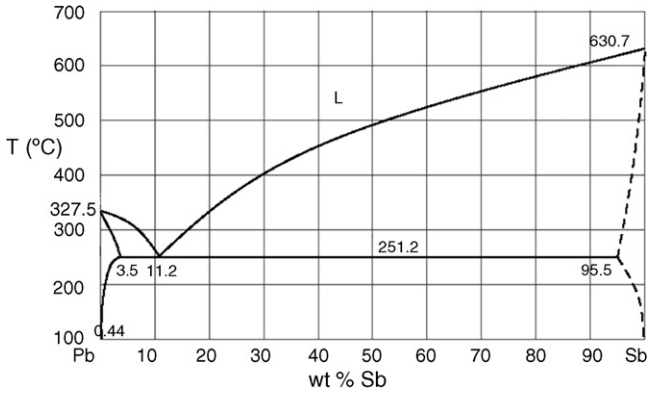

Fig. 4. Pb–Sb phase diagram.

surface (bottom) and a decreasing profile along the casting length (top) due to the increase of the thermal resistance of the solidified shell with distance from the cooled surface. This influence translates to the observed experimental values of cellular and dendritic spacings, with fine spacings close to the casting cooled surface (bottom) and coarser ones far from it (top). As can be observed in Fig. 3 the number of cells in a same area of analysis is remarkably distinct at transversal microstructures close to (5 mm) and far from (70 mm) the casting cooled surface. The typical microstructures observed along the cross-sections on both cellular and dendritic microstructures of the Pb–0.85 and 6.6 wt% Sb alloy castings are shown in Fig. 3a and b, respectively. The microstructure immediately after solidification consists of a completely cellular array for a solute content of 0.85 wt% Sb and a completely dendritic array for the Pb–6.6 wt% Sb alloy. Both microstructures are constituted by a Pb-rich matrix (α-phase: solid solution of Sb in Pb) with a eutectic mixture in the intercellular or interdendritic regions constituted of α, and a Sb-rich β-phase (solid solution of Pb in Sb). With the increase on the alloy solute content the eutectic fraction also increases, since the eutectic composition lies about 11.2 wt% Sb, as can be observed in the Pb–Sb phase diagram of Fig. 4.

3.2. Corrosion resistance of Pb–Sb cellular structures

It is well known that low solute content is one of the main factors favoring the formation of a cellular structure during solidification [13]. Generally, in conventional casting or continuous casting of Pb alloys grids, fine cellular structures are produced [1–9]. Particularly in the Pb–Sb system, such microstructural morphology consists of a Pb-rich cell core (with a hexagonal shape) and Sb-rich boundaries. These boundaries are regions of higher energy which is a result of distortions at the limits between adjacent cells during growth along the solidification process.

The corrosion behavior of a dilute Pb–0.85 wt% Sb alloy has been reported in a recent article [15]. It is shown that the resulting corrosion tendency is similar to that observed for pure metals with fine and large equiaxed grains [22,23]. The experimental EIS diagrams, potentiodynamic polarization curves and fitted equivalent circuit parameters have shown that coarser cellular

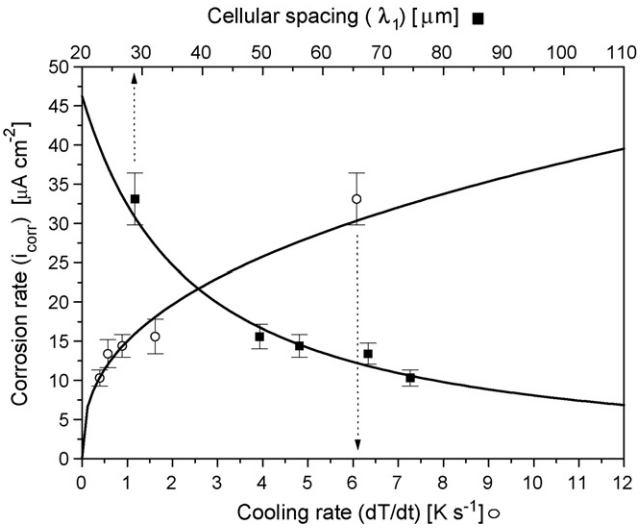

Fig. 5. Experimental corrosion rates of a dilute Pb–0.85 wt% Sb alloy as a function of cellular spacing and cooling rate during solidification.

structures tend to yield higher corrosion resistance than finer cellular structures. Such tendency of better corrosion resistance presented by coarser cells seems to be associated with the reduction of cellular boundaries when compared with finer cells, since the boundary has proved to be more susceptible to the corrosion action.

Fig. 5 shows the corrosion rate as a function of both cellular spacings (solid squares) and cooling rates during solidification (open circles) for the Pb–0.85 wt% Sb alloy. It can be seen that the corrosion rate decreases with increasing cell size. The cell size is imposed by the cooling rate during solidification, which is a thermal variable that depends on the operational conditions of the casting system. It can be seen in Fig. 5 that a corrosion rate of about 33 μA cm^{-2}, corresponds to values of cooling rate and cellular spacing of about 6 K s^{-1} and 28 μm, respectively. On the other hand, a corrosion rate of about 10 μA cm^{-2} can be related to a cooling rate and a cellular spacing of 0.4 K s^{-1} and 75 μm, respectively.

3.3. Corrosion resistance of Pb–Sb dendritic structures

In order to evaluate the corrosion behavior of a Pb–6.6 wt% Sb alloy, which has a dendritic pattern, experimental EIS results, including Bode and Bode-phase diagrams, potentiodynamic polarization curves and an equivalent circuit analysis have been used.

Fig. 6a and b shows the experimental EIS results in Bode and Bode-phase diagrams and potentiodynamic polarization curves, respectively, for samples collected at five different positions along the casting length. Both the modulus of impedance and the phase angle decrease with increasing distance from the casting bottom (casting/chill interface), as shown in Fig. 6a. As a direct consequence, both impedance and phase values decrease with increasing secondary dendrite arm spacings (λ_2). It is well known that higher impedance and phase angle are conducive to a nobler electrochemical behavior.

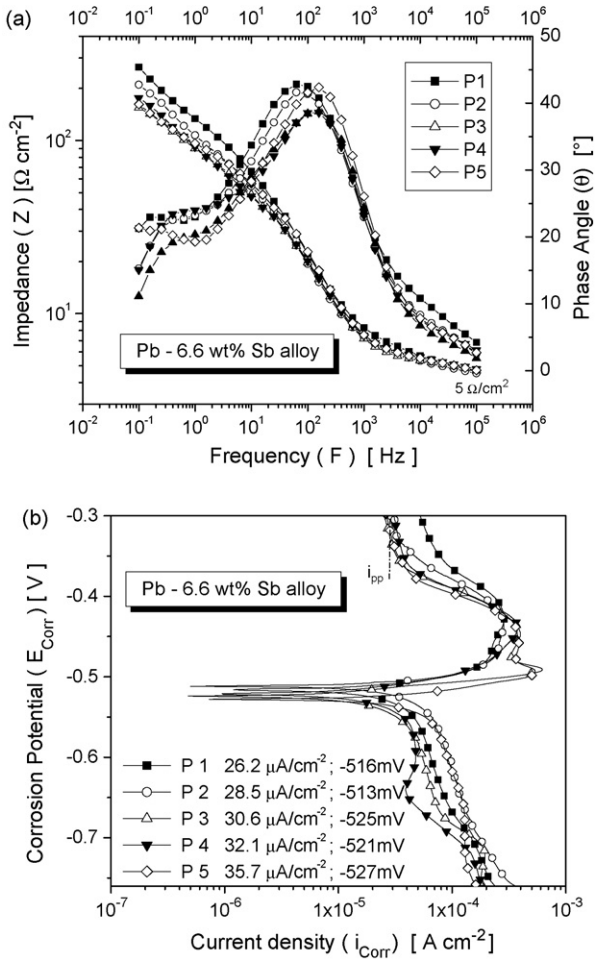

Fig. 6. (a) Experimental EIS test in Bode and Bode-phase diagrams. (b) Potentiodynamic polarization curves for a Pb–6.6 wt% Sb alloy as a function of secondary dendrite arm spacing.

The experimental EIS diagrams permit to see that the mechanism and the kinetics of corrosion action for all five positions experimentally examined are associated with at least two time constants. Similarly, the corresponding results for the Pb–0.85 wt% Sb alloy (cellular structure) have also shown two time constants. This effect has been attributed to the antimony segregation which is slightly different from bottom and top positions [15]. Both the Pb–6.6 wt% Sb and the Pb–0.85 wt% Sb castings exhibit typical normal macrosegregation profiles, as shown in Fig. 7.

Fig. 6b shows experimental potentiodynamic polarization curves for five different positions along the casting length. The corrosion current densities (i_{Corr}) were obtained from the polarization curves by Tafel plots using both cathodic and anodic branches of the polarization curves. Such results permit to reinforce the corrosion resistance tendency which has been observed when analyzing the experimental Bode and Bode-phase diagrams.

The corrosion current density (corrosion rate) at position P1 is lower than those of subsequent positions, as observed in Fig. 6b, i.e., the corrosion resistance decreases with increasing distance from the casting bottom.

In order to supply quantitative support for discussions of these experimental EIS results, an appropriate model (ZView® version 2.1b) for equivalent circuit quantification has also been used. Fig. 8 shows the equivalent circuit proposed to fit the experimental data and the examples of experimental and simulated agreement for positions P1 and P5 in Nyquist diagrams. The equivalent circuit is similar to that proposed by Mansfeld and Kendig to represent the oxide layer of anodized aluminium [24]. It has also been used by other researchers to represent different oxide layer formations [20,21].

The physical significance of the circuit elements has been reported in the literatures [15,20,21,25–27]. However, in the present investigation, for the mathematical analysis of impedance diagrams, a constant phase element, CPE, was used instead of an "ideal" capacitor and $Z_{CPE(1)}$, $Z_{CPE(2)}$ are defined as capacitances. The impedance parameters are shown in Table 1. The fitting quality was evaluated by Chi-squared (χ^2) values of about 10^{-4}, which were interpreted by the ZView software.

By analyzing the parameters in Table 1, it can be seen that position P1 (fine dendrite arm spacings) is associated to higher capacitances $Z_{CPE(1)}$ and higher polarization resistances R_1 if compared with those associated with increasing positions from the casting bottom. These results combined with the experimental EIS and the potentiodynamic polarization curves permit to conclude that, for the dendritic morphology a finer structure provides better corrosion resistance than a coarser one. In contrast,

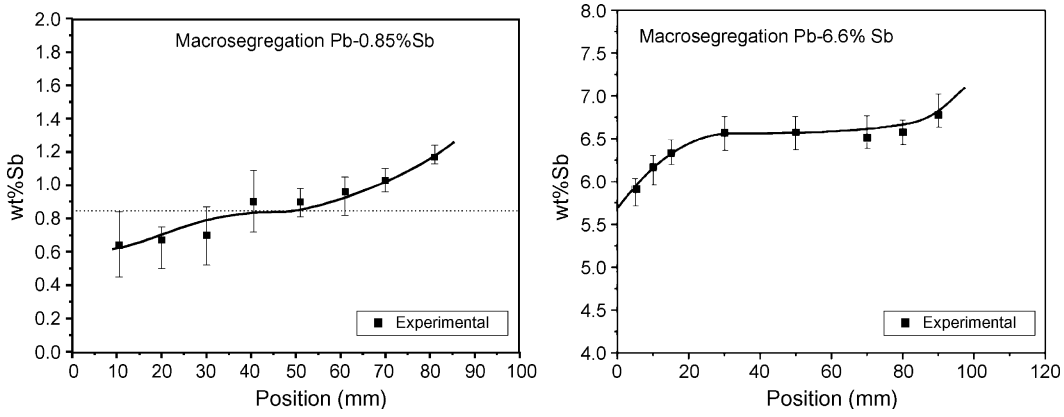

Fig. 7. Macrosegregation profiles along the castings length for Pb–0.85 wt% Sb and Pb–6.6 wt% Sb alloys.

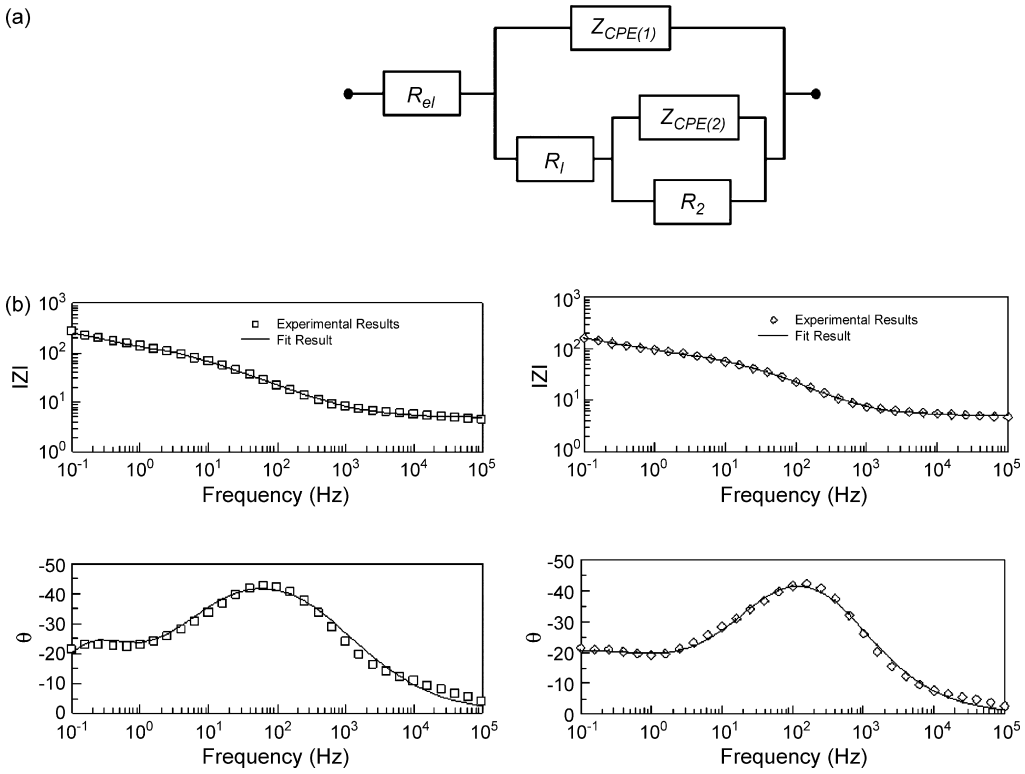

Fig. 8. (a) Equivalent circuit for modeling impedance data performed in a 0.5 M H_2SO_4 solution. (b) Experimental data and simulated curves by using the ZView® software for the Pb–6.6 wt% Sb alloy samples (positions P1 and P5 as shown in Fig. 2).

the opposite has been observed for cellular structures with finer cell regions being subjected to more intense corrosion action than coarser regions [15].

3.4. Differences in mechanisms and tendencies of corrosion resistance

In order to compare the mechanisms and tendencies of the corrosion action in cellular and dendritic structures, cooling rates during solidification, macrosegregation profiles and corrosion tests results have been analyzed. It was verified that the used water-cooled unidirectional solidification system has provided very similar cooling rates ($dT/dt = 32P^{-1}$) during solidification of both cellular and dendritic alloys, despite the different thermophysical properties and growth kinetics.

Poorer concentrations of antimony at regions closer to the casting bottom have been observed (relative to the nominal composition) for both cellular and dendritic morphologies, as shown in Fig. 7. Sb is nobler than Pb, but the analyses encompassed with both cellular and dendritic structures have shown that the variations on solute content (segregation profiles) have not significantly affected: (i) the range of modulus of impedance (same order of magnitude, 10^2 to $10^3\ \Omega\,cm^{-2}$), (ii) the corrosion potential (of about −500 mV) and (iii) the current density (from 10 to $30\ \mu A\,cm^{-2}$).

Although the Pb–6.6 wt% Sb alloy has a higher solute content compared to the dilute Pb–0.85 wt% Sb alloy, only a slight displacement on the corrosion potential to the more active side (less noble) has been verified for the Pb–6.6 wt% Sb alloy. The current densities (i_{Corr}) for the cellular structure casting have varied from 33 to $10\ \mu A\,cm^{-2}$ corresponding to finer spacings (casting bottom/higher cooling rate) and to coarser structures (casting top/lower cooling rate), respectively. On the other hand, for the dendritic structure casting, i_{Corr} has varied from 25 to

Table 1
– Impedance parameters for the Pb 6.6 wt% Sb alloy samples in a 0.5 M of H_2SO_4 solution

Parameters	P_1	P_2	P_3	P_4	P_5
R_{el} ($\Omega\,cm^{-2}$)	4.83	4.75	4.89	5.05	4.99
$Z_{CPE(1)}$ ($\times 10^6\ \Omega\,s^{-n}\,cm^2$)	854.03 (±12.4)	762.35 (±33.2)	572.13 (±55.1)	528.27 (±51.4)	425.41 (±37.5)
$Z_{CPE(2)}$ ($\times 10^3\ \Omega\,s^{-n}\,cm^2$)	5.89 (±0.4)	4.75 (±0.23)	4.68 (±0.26)	5.35 (±0.45)	9.4 (±1.1)
n_1	0.63	0.67	0.70	0.71	0.73
n_2	0.85	0.81	0.59	0.66	0.50
R_1 ($\Omega\,cm^{-2}$)	160	101	60	57	67
R_2 ($\Omega\,cm^{-2}$)	190	142	139	155	345
χ^2	20×10^{-4}	28×10^{-4}	24×10^{-4}	14×10^{-4}	19×10^{-4}

Values in parenthesis: error resulting from fitting the experimental data using the equivalent circuit.

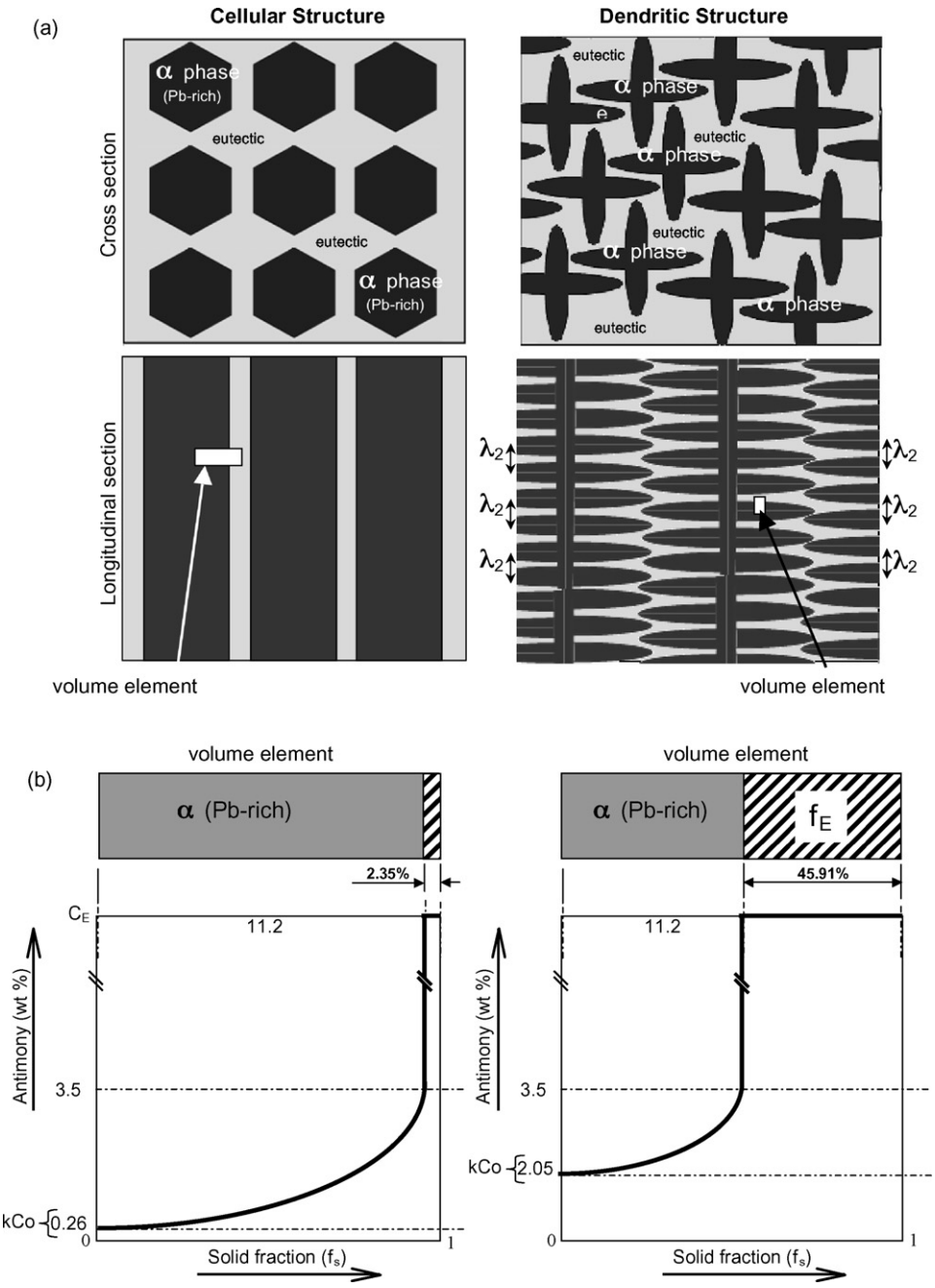

Fig. 9. (a) Schematic representation of the cellular and the dendritic arrangements: Pb–0.85 wt% Sb and Pb–6.6 wt% Sb alloys. (b) Volume elements and microsegregation profiles.

35 μA cm^{-2}, for fine (bottom) and coarse (top) dendritic structures, respectively.

The microstructure of hypoeutectic Pb–Sb alloys is constituted by a Pb-rich matrix (α-phase) of increasing Sb content from the matrix core involved by a eutectic mixture formed by a lamellar alternation of β-phase (solid solution of Sb in Pb) and α-phase (Pb-rich).

The morphological shapes of the Pb-rich phase/eutectic mixture for cells and dendrites are shown schematically in Fig. 9a. As the microsegregation phenomenon is associated to each microstructural pattern it is convenient to analyze separately Pb–Sb cellular and dendritic alloys, as shown in Fig. 9.

By assuming that the equilibrium partition coefficient is constant, it can be calculated at the eutectic temperature (252 °C), i.e., $k = C_S/C_L = 3.5/11.2 = 0.31$, as can be observed in the Pb–Sb phase diagram (Fig. 4). Such parameter can be used into Scheil's equation [28] to estimate the eutectic fraction (f_E) formed during non-equilibrium solidification of both Pb–Sb alloys: Pb–0.85 wt% Sb, $f_E = 2.35\%$ and Pb–6.6 wt% Sb, $f_E = 45.91\%$. The calculated microsegregation profiles are shown in Fig. 9b for both alloys.

The dendritic microstructure of a Pb–Sb alloy is mainly formed by α-phase (less noble) and the interdendritic region has a lamellar eutectic morphology (mixture of α- and β-phases). It seems that the corrosion action preferentially occurs at the Pb-rich dendritic matrix which is more corrosion active than the interdendritic region (Sb-rich nobler region). A more extensive distribution of the Pb-rich dendritic matrix (less noble regions) which is associated to smaller dendritic spacings will have the eutectic mixture which contains the nobler Sb-rich phase "enveloping" the Pb-rich regions, and thus providing a better corrosion resistance. A coarser dendritic structure will have the larger Pb-rich regions more exposed and thus favoring the corrosion action.

Fig. 10 shows an optical micrograph and a schematic representation of a typical lamellar eutectic mixture formed by α_E-phase (Pb-rich with 3.5 wt% Sb) and β-phase (Sb-rich with 95.5 wt% Sb).

Fig. 11 shows the corrosion rate of Pb–0.85 and 6.6 wt% Sb alloy samples as a function of position from the casting bottom. It has been shown in Fig. 2a that cell and dendrite spacings increase from bottom to top. For the dilute alloy (cellular arrangement), the corrosion rate increases with decreasing cell size. In contrast, for the Pb–6.6 wt% Sb alloy (dendritic arrangement), the corrosion rate decreases with decreasing dendritic arm spacings.

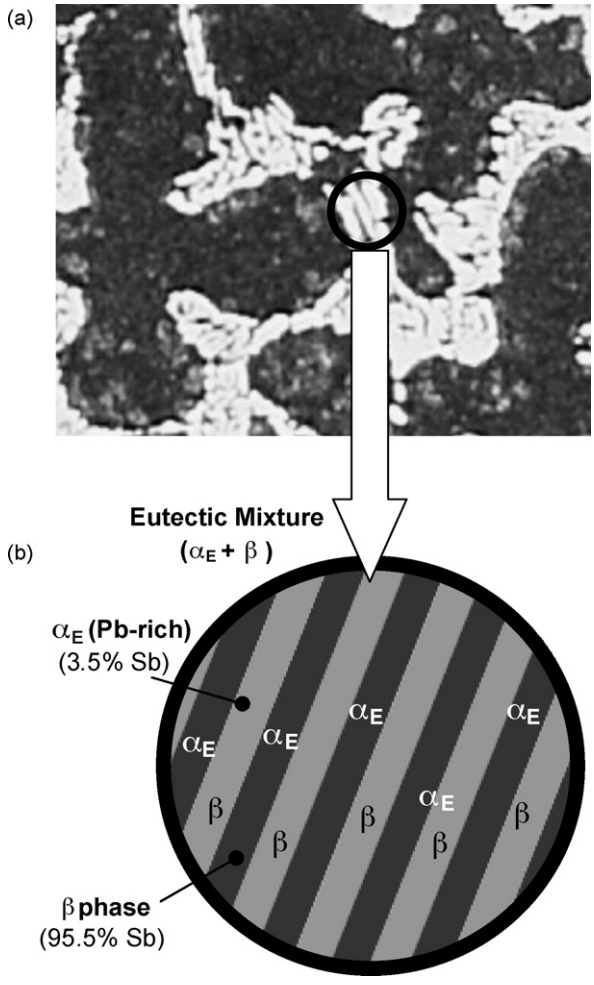

Fig. 10. (a) Typical micrography of a Pb–6.6 wt% Sb alloy. (b) Schematic representation evidencing the lamellar eutectic mixture.

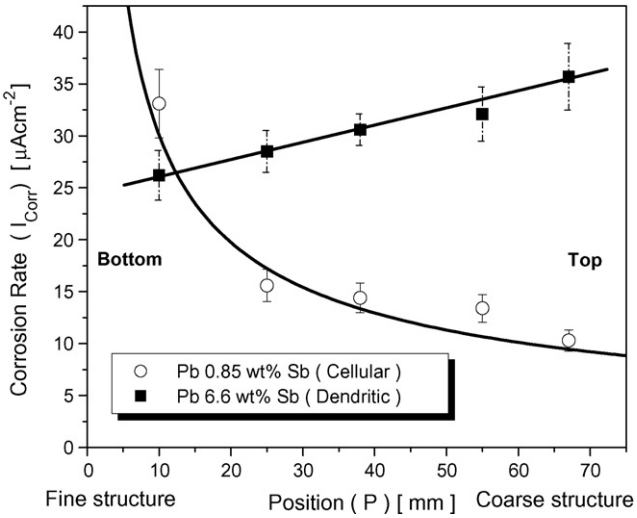

Fig. 11. Experimental corrosion rates of Pb–0.85 wt% Sb and Pb–6.6 wt% Sb alloy samples as a function of position from the casting bottom.

The present experimental results have shown that the operational conditions of the casting system can be used to the control of cooling rate and hence can be used as an alternative way to produce as-cast Pb–Sb grids for lead acid batteries with better corrosion behavior. In the production of as-cast grids of Pb–Sb alloys, a low solute content alloy has to be associated to a conventional casting process (low cooling rate and coarse cell morphology), so that a better corrosion behavior can be attained. For dendritic Pb–Sb alloys, a continuous casting process which provides a finer dendritic morphology (and a better corrosion behavior) is more appropriate. The present experimental investigation has indicated that a solute content up to 3 wt% Sb is conducive to a cellular morphology and that for alloys with antimony contents superior to 3 wt%, a dendritic pattern is expected.

4. Conclusions

The present experimental investigation permits the following conclusions to be drawn:

- The experimental EIS diagrams, potentiodynamic polarization curves and fitted equivalent circuit parameters have shown that coarser cellular structures and finer dendritic arrays tend to yield higher corrosion resistances than finer cellular structures and coarser dendritic structures for hypoeutectic Pb–Sb alloys. In the case of cellular morphologies, such tendency of better corrosion resistance presented by coarser cells seems to be associated with the reduction of cellular boundaries when compared with finer cells, since the boundary has proved to be more susceptible to the corrosion action. On the other hand, the dendritic array morphology has the antimony-rich regions located in the lamellar eutectic mixture. The Sb-rich lamellae will envelope the Pb-rich phase more efficiently for finer dendritic spacings due to the more

extensive distribution of the eutectic mixture, and thus protecting the Pb-rich matrix.

- Conventional casting processes with low cooling rates will be more appropriate for the manufacturing of low Sb alloy grids (<3 wt% Sb), since the resulting coarse cell morphology will have a higher corrosion resistance. For Pb–Sb dendritic alloys (>3 wt% Sb) finer dendritic spacings which are typical of a continuous casting process would be more appropriate due to the expected higher corrosion resistance.
- An alternative way to produce as-cast Pb–Sb alloys battery grids with improvements on the corrosion resistance can be achieved by controlling the cooling rate during casting, i.e., by pre-programming the solidification processing variables.

Acknowledgements

The authors acknowledge financial support provided by FAPESP (The Scientific Research Foundation of the State of São Paulo, Brazil), FAEPEX-UNICAMP and CNPq (The Brazilian Research Council).

References

[1] M.D. Achtermann, M.E. Greenlee, J. Power Sources 33 (1991) 87–92.
[2] J. Wirtz, Batteries International, January 1996, p. 56.
[3] R.D. Prengaman, J. Power Sources 95 (2001) 224–233.
[4] R.D. Prengaman, in: K.R. Bullock, D. Pavlov (Eds.), Advances in Lead-Acid Batteries, vol. 84-14, The Electrochemical Society, Pennington, NJ, 1984, p. 201.
[5] G.S. Al-Ganainy, M.T. Mostafa, F. Abd El-Salam, Physica B 348 (2004) 242–248.
[6] B. Rezaei, S. Damiri, J. Solid State Electrochem. 9 (2005) 590–594.
[7] M. Shiota, T. Kameda, K. Matsui, N. Hirai, T. Tanaka, J. Power Sources 144 (2005) 358–364.
[8] P.S. Kolisnyk, J. Power Sources 38 (1992) 59–61.
[9] L. Yu, G.L. Ding, J. Reye, S.N. Ojha, S.N. Tewari, Metall. Mater. Trans. A 30A (1999) 2463–2471.
[10] S.P. O'Dell, G.L. Ding, S.N. Tewari, Metall. Mater. Trans. A 30A (1999) 2159–2165.
[11] J. Hui, R. Tiwari, X. Wu, S.N. Tewari, R. Trivedi, Metall. Mater. Trans. A 33A (2002) 3499–3510.
[12] J. Chen, S.N. Tewari, G. Magadi, H.C. de Groh III, Metall. Mater. Trans. A 34A (2003) 2985–2990.
[13] D.M. Rosa, J.E. Spinelli, I.L. Ferreira, A. Garcia, J. Alloy Compd. 422 (2006) 227–238.
[14] W.R. Osório, P.R. Goulart, G.A. Santos, C. Moura Neto, A. Garcia, Metall. Mater. Trans. 37A (2006) 2525–2537.
[15] D.M. Rosa, J.E. Spinelli, W.R. Osório, A. Garcia, J. Power Sources 162 (2006) 696–705.
[16] G. Song, A.L. Bowles, D.H. StJohn, Mater. Sci. Eng. A 366 (2004) 74–86.
[17] W.R. Osório, C.M.A. Freire, A. Garcia, J. Mater. Sci. 40 (17) (2005) 4493–4499.
[18] W.R. Osório, J.E. Spinelli, N. Cheung, A. Garcia, Mater. Sci. Eng. A 420 (2006) 179–186.
[19] W.R. Osório, P.R. Goulart, A. Garcia, Mater. Lett., in press, doi:10.1016/j.matlet.2007.05.051.
[20] D. Pavlov, M. Bojinov, T. Laitinen, G. Sundholm, Electrochim. Acta 36 (1991) 2087–2092.
[21] D. Pavlov, M. Bojinov, T. Laitinen, G. Sundholm, Electrochim. Acta 36 (1991) 2081–2086.
[22] W.R. Osório, C.M.A. Freire, A. Garcia, J. Alloy Compd. 397 (2005) 179–191.
[23] W.R. Osório, C.A. Siqueira, C.M.A. Freire, A. Garcia, Rev. Metalurgia Madrid Extr. (2005) 176–180.
[24] F. Mansfeld, M.W. Kendig, J. Electrochem. Soc. 135 (1988) 828–835.
[25] J. Pan, D. Thierry, C. Leygraf, Electrochim. Acta 41 (1996) 1143–1153.
[26] M. Kliskic, J. Radosevic, S. Gudic, M. Smith, Electrochim. Acta 43 (1998) 3241–3255.
[27] S. Gudic, J. Radosevic, M. Kliskic, Electrochim. Acta 47 (2002) 3009–3016.
[28] W. Kurz, D.J. Fisher, Fundamentals of Solidification, Trans. Tech. Publications, Switzerland, 1992.